

ADDITIVE MANUFACTURING OF METALS: COMPLEX MICROSTRUCTURES AND ARCHITECTURE DESIGN

Experimental and numerical investigation of selective laser melting–induced defects in Ti–6Al–4V octet truss lattice material: the role of material microstructure and morphological variations

Asma El Elmi¹, David Melancon², Meisam Asgari³, Lu Liu¹, Damiano Pasini^{1,a)}

¹Mechanical Engineering Department, McGill University, Montreal, Quebec H3A 0C3, Canada

²John A. Paulson School of Engineering and Applied Sciences, Harvard University, Cambridge, Massachusetts, USA

³School of Engineering and Applied Science, Northwestern University, Evanston, Illinois, USA; and Mechanical Engineering Department, McGill University, Montreal, Quebec H3A 0C3, Canada

^{a)}Address all correspondence to this author. e-mail: damiano.pasini@mcgill.ca

Received: 1 February 2020; accepted: 12 March 2020

The remarkable progress in additive manufacturing has promoted the design of architected materials with mechanical properties that go beyond those of conventional solids. Their realization, however, leads to architectures with process-induced defects that can jeopardize mechanical and functional performance. In this work, we investigate experimentally and numerically as-manufactured defects in Ti–6Al–4V octet truss lattice materials fabricated with selective laser melting. Four sets of as-manufactured defects, including surface, microstructural, morphological, and material property imperfections, are characterized experimentally at given locations and orientations. Within the characterized defects, material property and morphological defects are quantified statistically using a combination of atomic force microscopy and micro-computed tomography to generate representative models that incorporate individual defects and their combination. The models are used to assess the sensitivity to as-manufactured defects. Then, the study is expanded by tuning defects amplitude to elucidate the role of the magnitude of as-designed defects on the mechanical properties of the lattice material.

Introduction

The emerging field of architected materials, whose properties are determined by their microarchitecture rather than the properties of the solid constituents, has led to dramatic progress in material design. In the context of bone-interfacing orthopaedic implants, architected materials are especially desirable to meet stringent biological requirements and attain superior mechanical performance [1, 2, 3]. Such demands often lead to material architectures that feature complex structural geometry often inaccessible to traditional manufacturing methods such as direct metal foaming or vapor deposition [4]. Recent progress in powder bed fusion (PBF) processes, such as selective laser melting (SLM) and electron beam melting (EBM), has enabled the fabrication of porous materials with controlled morphological parameters [5, 6, 7, 8].

Despite the high precision offered by these processes, several imperfections arise during the fabrication of complex

porous metals, thereby affecting their mechanical properties and functionality, such as bone ingrowth. PBF-induced defects typically depend on the physics of the fabrication technology along with its process parameters, such as laser power, scan speed, layer thickness, base power, and chamber environment [9, 10]. They can be classified into (i) surface flaws, (ii) microstructural and (iii) material property imperfections, and (iv) dimensional inaccuracies.

The first set of defects, surface flaws, arises from the interaction of the powder material with the energy source [11]. This can lead to an unstable melted pool of material that induces balling and bonded particles as well as stair-step effect whose magnitude depends on the type of manufacturing process, i.e., the SLM surface is smoother than the EBM counterpart [9], and building orientation, i.e., the surfaces with continuous variation of the inclination angles [11], are less

prone to surface defects. Surface porosity can also be observed in nonpolished samples [12].

Second, microscopic defects, e.g., irregularities of the microstructure including porosity [13], cracks [14, 15], and variation of the grain orientation [12], can also be found in porous metals built via Additive Manufacturing (AM) [11]. Pores induced by SLM are generally spherical, with a diameter of less than 100 μm [11, 12, 13, 14, 15, 16]. Depending on the manufacturing parameters, pores can appear with more prominent concentration, either in the nodes [17] or in the struts [9]. They are also dependent on the strut slenderness with higher statistical occurrence of porosity in low slenderness struts [13] and at lower inclination [18]. The pores are found to increase in larger unit cells because longer scanning paths provide more time for the pores to form [19]. The number of defects has also been found to be lower in EBM samples compared to their SLM counterparts [9]. More irregular voids containing unmelted powder have been also observed to be caused by insufficient input energy [16].

Third, material property defects depend on the manufacturing technique and on the building orientation. Parts that are built with EBM techniques possess a higher Young's modulus than their SLM counterparts [9], and parts that are oriented at a lower inclination angle with the building direction are stiffer than the ones that are built orthogonal to the building direction [13]. Their mechanical properties have been measured through uniaxial testing [13]; however, the role of their local distribution has not been investigated yet.

The fourth set of defects, dimensional inaccuracies, corresponds to deviations from nominal geometry. Although they are typically reported for the struts [20, 21], a paucity of works exists aiming at characterizing dimensional inaccuracies at the nodes and investigating their impact [22]. Struts possess varying thickness [23], waviness [24], and a deviation from circular to ellipsoidal cross section due to over melting [25]. These discrepancies are highest at the borders of the strut and depend on the orientation of the struts to the building direction [24].

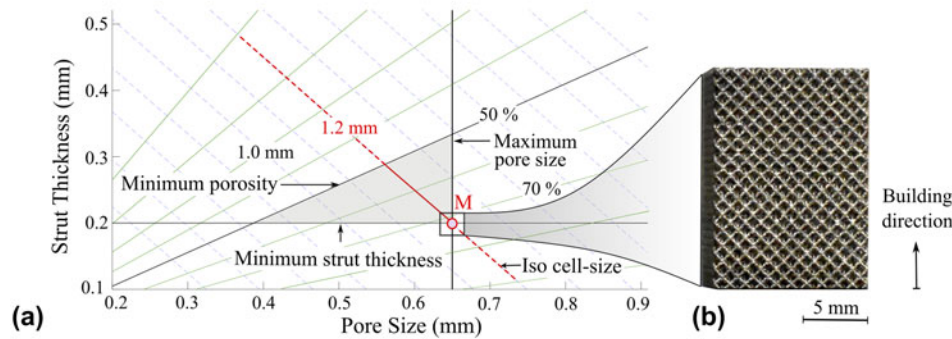
Several works have studied the role of defects on the effective properties of 2D and 3D lattices including Young's modulus [26, 27], yield strength [28, 29], and fracture toughness [30, 31]. Defects can arise from manufacturing (i.e., as-manufactured defects) or can be intentionally introduced in the lattice (i.e., as-designed defects) [31, 32]. The sensitivity to defects depends not only on the geometrical characteristics of the lattice structure (cell topology, nodal connectivity, and unit cell dimensions), but also on the base material that constitutes it [31]. On the characterization front, there exist several techniques capable to experimentally investigate as-manufactured defects in lattice materials. Established methods, such as optical microscopy [33, 34] and scanning electron microscopy

(SEM) [35, 36], have been used to inspect microstructural imperfections, surface defects, and qualitatively dimensional inaccuracies. Electron backscatter diffraction (EBSD) analysis has enabled to shed light on microstructure defects, such as the variation of the grain orientation [12]. Micro-computed tomography ($\mu\text{-CT}$) has been used to quantify dimensional inaccuracies, such as strut waviness and strut thickness variation [37]. High-resolution experimental methods, such as atomic force microscopy (AFM), can unveil information on the material property distribution [38]; however, these techniques have not been used to characterize material property distribution in metallic lattices.

The impact of as-designed and as-manufactured defects also depends on the base material properties and cell connectivity. In elastic lattices, increasing strut waviness decreases the Young's modulus of stretching dominated structures, but it has minor impact on bending dominated lattices [39]. Rigid inclusions have negligible impact on elastic honeycombs in comparison with missing cell walls, thereby reducing significantly bulk modulus [31, 32, 33, 34, 35, 36, 37, 38, 39, 40], Young's modulus, and yield strength because missing cell walls induce an additional degree of bending [41]. In elastoplastic honeycombs under biaxial loading, the fractured cell wall can have a large impact on yield strength because such a defect induces a switch of deformation mode from cell wall stretching to cell wall bending [29]. For instance, the variation of the thickness ratio of horizontal to diagonal struts in an octet truss lattice induces a failure mode that switches from shear band to horizontal crushing [24]. Finally, in elastobrittle lattices, the increase of nodal connectivity increases the fracture toughness [42].

Although as-manufactured dimensional inaccuracies of the struts have been studied in the literature [24], no study has so far focused on dimensional variations at the nodes. Furthermore, the role of the base material property distribution in cellular materials built via AM remains unexplored and its characterization requires novel experimental approaches. In this article, we focus on four sets of as-manufactured defects, including those so far unexplored: microstructural, surface, material property, and morphological defects characterized at given locations and orientations inside the lattice architecture. We propose a general methodology for the quantification of selected defects and their integration in imperfect models that shed light onto the impact they bring in the elastic response of lattice materials. The methodology is demonstrated here by applying it to cellular materials satisfying geometric constraints for additive manufacturing and bone ingrowth requirements [Fig. 1(a)]. The method combines AFM and X-ray $\mu\text{-CT}$ to obtain a statistical distribution of material property and morphological defects of the struts [Fig. 1(e)] and the nodes [Fig. 1(f)]. We expand the study by introducing as-designed

○ Manufacturing



○ Characterization of defects

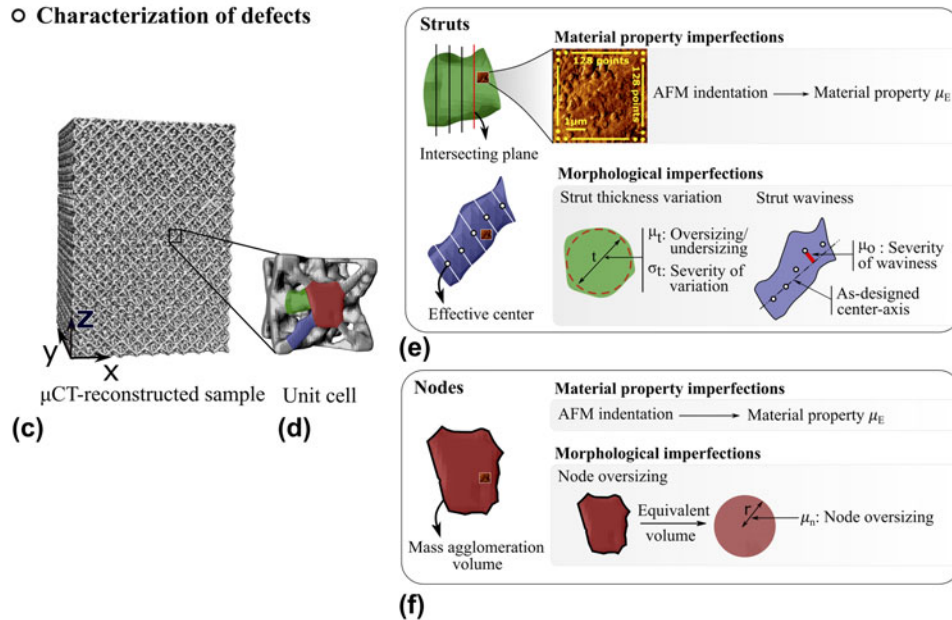


Figure 1: Sample manufacturing: (a) Visualization of the design space (triangle highlighted in grey) that satisfies bone ingrowth and additive manufacturing constraints, and the 1.2 mm selected cell size under investigation (red line), (b) manufactured sample corresponding to the selected manufacturing point M. Schematic of defects characterization: (c) μ -CT reconstructed sample with a zoom on (d) μ -CT reconstructed unit cell highlighting a horizontal strut (oriented 90° with respect to building direction and highlighted in green), a diagonal strut (oriented 45° with respect to building direction and highlighted in blue) and a node (highlighted in red). Material property and morphological defects are extracted for (e) the struts and (f) the nodes.

defects with tuned amplitude. The study of the impact of as-manufactured defects and as-designed defects allows to gain insight into the influence of mass and material property distribution on the mechanical properties of 3D lattice materials.

Experimental results

Here, we report the main findings of our experimental campaign. We first describe the design and manufacturing of our lattice samples, followed by results from the experimental characterization of their surface, microstructure, morphology and solid material properties.

Design and samples manufacturing

Cellular materials can be classified into stretching or bending dominated structures depending on their node connectivity

[43]. The octet truss cell topology, a stretching dominated structure with cubic symmetry, was here selected for its high specific stiffness and strength, distinctive requirements of load-bearing applications [23]. This cell topology was recently studied to assess the admissible design space that satisfies manufacturing and bone ingrowth constraints [21]. Figure 1(a) shows its geometric domain defined by isometric lines of porosity and cell size, highlighted in green and dashed blue, respectively, and of pore size and strut thickness. The admissible design space for the octet truss that satisfies additive manufacturing requirements [5, 6] (200 μ m minimum strut thickness) and bone ingrowth requirements [21] (a 50% minimum porosity and a pore size between 50 and 650 μ m) is a triangular domain that is highlighted in grey [Fig. 1(a)]. In this study, we prescribed the cell size to 1.2 mm [red line in Fig. 1(a)].

Samples were manufactured in 10 replicates with design parameters corresponding to the design point M [Fig. 1(a)]. Relevant design parameters are summarized in Table SI in the Supplementary material. Manufacturing was made via SLM from Ti-6Al-4V powder (Renishaw AM-250), with powder size ranging from 15 to 50 μm and a 30- μm powder layer thickness using a 200 W laser with 60 J/mm³ energy density and 70 μm spot diameter. Fabrication was performed under argon atmosphere to avoid composition change due to oxidation and was followed by annealing at 730 °C for 2 h. The samples were extracted from the building plate using electrical discharge machining. Figure 1(b) shows the manufactured sample. A relative density (i.e., the density of the cellular material divided by that of the constituent material, which corresponds to the volume fraction) of $\bar{\rho} = 0.34 \pm 0.025$ was assessed for the manufactured samples by measuring their mass and their apparent volume. The samples were tested in compression to determine their compressive Young's modulus, which was found to be equal to 3 ± 2 GPa.

Characterization of surface defects

Surface defects correspond to irregularities in the unpolished surface of the samples. SEM (Hitachi UHR Cold-Emission FE-SEM SU8000) with 15 kV as the operating condition was used to assess the surface quality of the manufactured samples. In Fig. 2, we show a representative portion of the octet truss lattice highlighting a nonsmooth surface as well as several defects arising from the interaction between powder material and energy source [11]. One of such defects is in the form of powder particles bonded to the surface of the lattice struts. These spherical particles, whose diameter varies from a few micrometers to 90 μm with 40 μm average size, result from the unstable melt pool and induce a rough surface finish to the printed part (Fig. 2). Furthermore, we can observe the stair-step effect that typically appears in layer-wise fabrication, contributing to poor surface finish quality. In our study, a 30- μm layer thickness was used to minimize this defect that is mainly observed on the struts. Finally, surface pores with a spherical shape and an approximate diameter of 80 μm were identified on our fabricated samples.

Characterization of microstructural defects

Microstructural defects correspond to irregularities of the microstructure including porosity, cracks, and variation of the texture. We reveal these defects using a combination of SEM, EBSD analysis, and AFM. In our study, we focus on the local variation (struts versus nodes) of the microstructure and its dependence on the orientation (horizontal versus diagonal struts). Specimens were cut using a diamond blade with a cutting plane perpendicular to the building direction at given

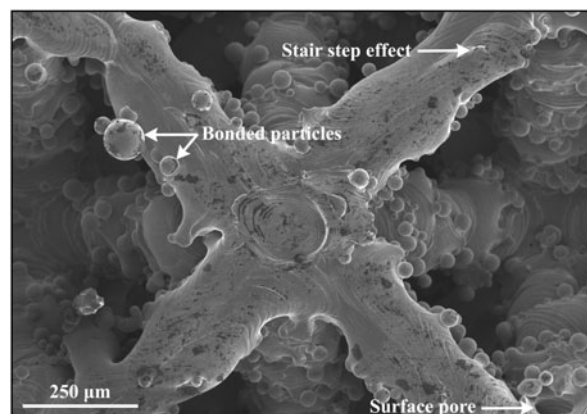


Figure 2: SEM image of a representative region of the manufactured sample showing typical surface defects due to the manufacturing: bonded particles, stair-step effect, and surface porosity.

positions within the lattice. Figures 3(a) and 3(f) show schematic positions of the cutting planes that reveal both the horizontal strut and the node for the first position and the diagonal strut for the second position.

The sections were polished using silicon carbide abrasive paper and 3 μm diamond paste followed by a final polishing using alumina silica with acid. We performed SEM analysis on these sections [see Figs. 3(b) and 3(g)] to investigate microstructural defects. In particular, on the diagonal strut, we found pores having 10–30 μm diameter. We also found cracks of 5 μm approximate thickness which initiated due to the residual stresses that typically arise from the rapid expansion and contraction of the material under the high thermal gradients [16].

We characterized the grain morphology and the texture using an EBSD system installed on Hitachi SU3500 SEM with 15 kV as the operating condition and analyze the EBSD data with Aztec data acquisition software combined with HKL Channel 5. EBSD maps were generated for the two highlighted regions shown in Figs. 3(b) and 3(g) based on the crystallographic parameters of the titanium hexagonal phase using 0.6 and 0.25 μm step size, respectively. Figures 3(c) and 3(h) show the EBSD results indicating elongated grains and a heterogeneous polycrystalline structure. Figures 3(d), 3(e), and 3(i) show the pole figures obtained from the EBSD measurements at the highlighted locations in EBSD maps in Figs. 3(c) and 3(h). The color code on the right of the pole figures shows the level of multiples of uniform distribution (MUD). The texture is found to depend on the strut orientation as shown in the pole figure of the horizontal strut [Fig. 3(d)] and the diagonal strut [Fig. 3(i)]. A strong texture was observed in the node in the (0001) plane where a 14.78 times random intensity was recorded [Fig. 3(e)]. The spatial variations of the texture can be attributed to temperature gradients caused by the manufacturing process.

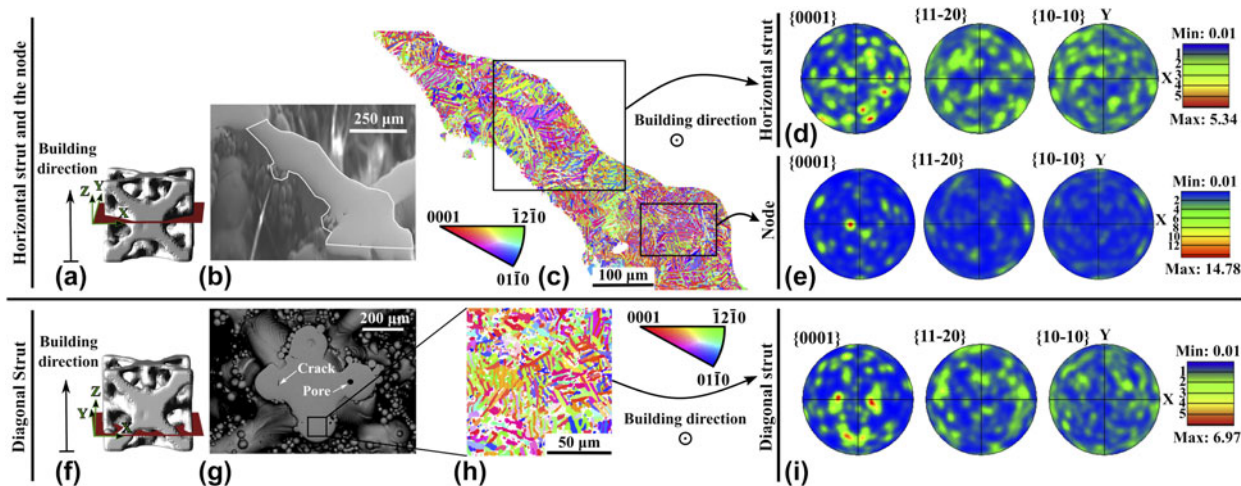


Figure 3: Microstructure investigation: (a) Transverse section of a representative μ -CT reconstructed unit cell revealing (b) a horizontal strut and node along with its (c) EBSD micrograph and pole figures for (d) the horizontal strut and (e) the node. (f) Transverse section revealing (g) a diagonal strut with (h) EBSD micrograph (h) along with (i) respective pole figures. The color code on the right of the pole figures shows the level of MUD.

To obtain a higher resolution images of the microstructure, AFM was used (see section “Methods” for details) at given regions in the nodes and in the struts. Porosity and poor bonding defects were observed mostly in the struts rather than in the nodes. Figure 4(a) shows an AFM observation in the node, and Fig. 4(e) reveals a poor bonding defect in the strut. The defect size is approximately $4\ \mu\text{m}$ and is the result of an insufficient molten metal during the solidification process.

Characterization of material property defects

In this section, we explore material property defects using AFM and quantify their distribution statistically in the nodes, the horizontal struts, and the diagonal struts. These defects correspond to the local variation of Young’s modulus and its dependence on the orientation. A similar approach to the one used in the previous section was used to examine horizontal struts, diagonal struts, and nodes. We used a JPK atomic force microscope (JPK Nano-wizard@3 Bio-Science, Berlin, Germany) to conduct a set of nano-indentation tests on the transverse sections, which were previously polished to minimize surface roughness ($<5\ \text{nm}$). Figures 4(c), 4(g), and 4(i) show schematics of the indentation region at the node and the horizontal and diagonal struts, respectively. Force maps containing 16,384 indentation points were generated on each indentation area as shown in Fig. 4(b) points among them with acceptable force–deflection curves were selected. To better capture the material property distribution, 18, 19, and 26 transverse sections were cut at given levels within the samples, resulting in a total of 198,216, 155,138, and 239,914 points being tested in the horizontal struts, the diagonal struts, and the nodes, respectively. Table SII in the Supplementary material summarizes the indentation data.

Figures 4(d), 4(h), and 4(j) show histograms of the probability distribution versus Young’s modulus in the nodes, the horizontal and the diagonal struts. The histogram represents the probability of the measured data, and the red line corresponds to the normal probability density function. Three sets of material property defects were characterized:

- (i) Variation of the diagonal strut material property describes the material stiffening from the nominal value ($E = 114\ \text{GPa}$) of the diagonal struts which reaches the highest value of $121.84\ \text{GPa}$. The mean value of the measured Young’s modulus is equal to $\mu_E^d = 118\ \text{GPa}$, and the standard deviation is equal to $\sigma_E^d = 1.8\ \text{GPa}$.
- (ii) Variation of the horizontal strut material property describes the material softening from the nominal value ($E = 114\ \text{GPa}$) of the horizontal struts which reaches the lowest value of $105.54\ \text{GPa}$. The mean value of the measured Young’s modulus is $\mu_E^h = 111\ \text{GPa}$, and the standard deviation is equal to $\sigma_E^h = 3.4\ \text{GPa}$.
- (iii) Variation of the node material property describes the material stiffening from the nominal value of the nodes which reaches the highest value of $131.25\ \text{GPa}$. The mean value of the measured Young’s modulus is equal to $\mu_E^n = 125\ \text{GPa}$, and the standard deviation is equal to $\sigma_E^n = 3.8\ \text{GPa}$. As shown in the three sets of defects, SLM induces material properties with important spatial variation. Enhanced properties are obtained in the diagonal struts and particularly in the nodes, whereas lower Young’s modulus values are observed in the horizontal struts. The nodes tend to be the stiffest constitutive parts with Young’s modulus that is 13% and 6% higher than the horizontal and diagonal struts, respectively. This deviation can be attributed to material

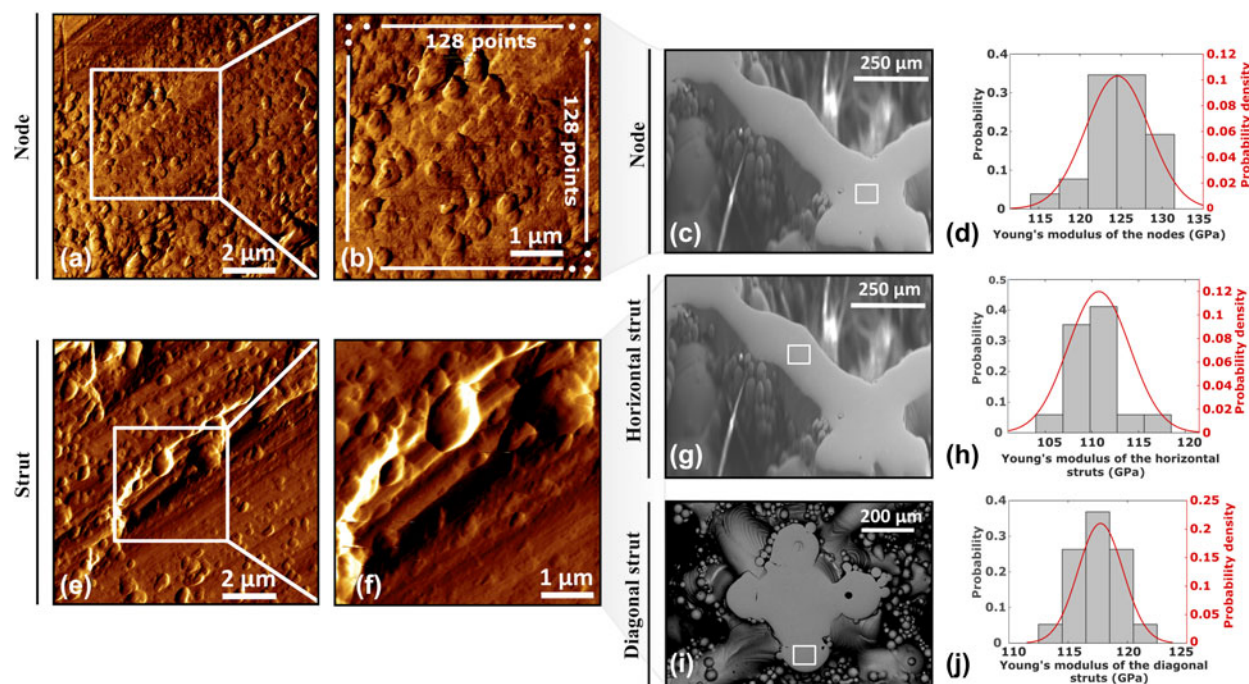


Figure 4: AFM investigation: Representative AFM images in (a) the node with a zoom on (b) the indentation area. AFM images in (e) the strut with a zoom on (f) the poor bonding defect. Schematic of the indentation region in representative areas: (c) a node, (g) a horizontal strut, and (i) a diagonal strut. Probability density distributions of Young's modulus obtained by performing several indentations at (d) the nodes, (h) horizontal struts, and (j) diagonal struts.

texture, molecular bonding, and nano porosities in the solid material. As previously shown, the nodes feature a strong texture along the building direction and, in our study, were found to possess the highest Young's modulus when indented along this direction.

Characterization of morphological defects

Morphological defects correspond to deviations from the nominal geometry of the material architecture. To characterize them, we first resorted to SEM, and, then, captured their statistical distributions in μ -CT reconstructed lattices [Fig. 1(c)]. The μ -CT-reconstruction was made using semi-automated segmentation under ITK-SNAP out of CT-scanned data (SkyScan 1172 high-resolution μ -CT). Further details about the morphological characterization of defects can be found in "Methods" section. Three sets of morphological defects were characterized:

- (i) Strut thickness variation corresponds to the cross-sectional deviation from the nominal circularity along the strut length. Figure 5(a) shows SEM observation of the defect, and Figs. 5(b) and 5(c) show the probability distribution of the thickness variation in horizontal and diagonal struts, respectively. The standard deviation σ_t of the strut thickness represents the severity of the strut

thickness variation, and the mean value μ_t represents the oversizing or undersizing of the strut. For the horizontal strut [Fig. 5(b)], $\mu_t^h = 0.2$ mm and $\sigma_t^h = 0.029$ mm. For the diagonal strut [Fig. 5(c)], $\mu_t^d = 0.15$ mm and $\sigma_t^d = 0.019$ mm. Therefore, the diagonal struts are in general undersized in comparison with the horizontal struts.

- (ii) Strut waviness characterizes the center-axis misalignment of the manufactured strut from its nominal position. Figure 5(d) shows an SEM observation of the defect, and Figs. 5(e) and 5(f) show the probability distribution of the strut waviness for the horizontal and the diagonal struts, respectively. The mean value μ_o indicates the average center-axis misalignment, and the standard deviation σ_o represents the variation of the strut center-axis offset. For the horizontal strut [Fig. 5(e)], $\mu_o^h = 0.018$ and $\sigma_o^h = 0.01$. For the diagonal strut [Fig. 5(f)], $\mu_o^d = 0.01$ mm and $\sigma_o^d = 0.007$ mm.
- (iii) Node size variation characterizes the node oversizing due to mass agglomeration accrued during manufacturing at the intersection between struts. Figure 5(g) shows SEM observation of an isolated mass agglomeration at the node, and Fig. 5(h) shows the probability density distribution of its equivalent node radius. The mean value $\mu_n = 0.3$ mm corresponds to

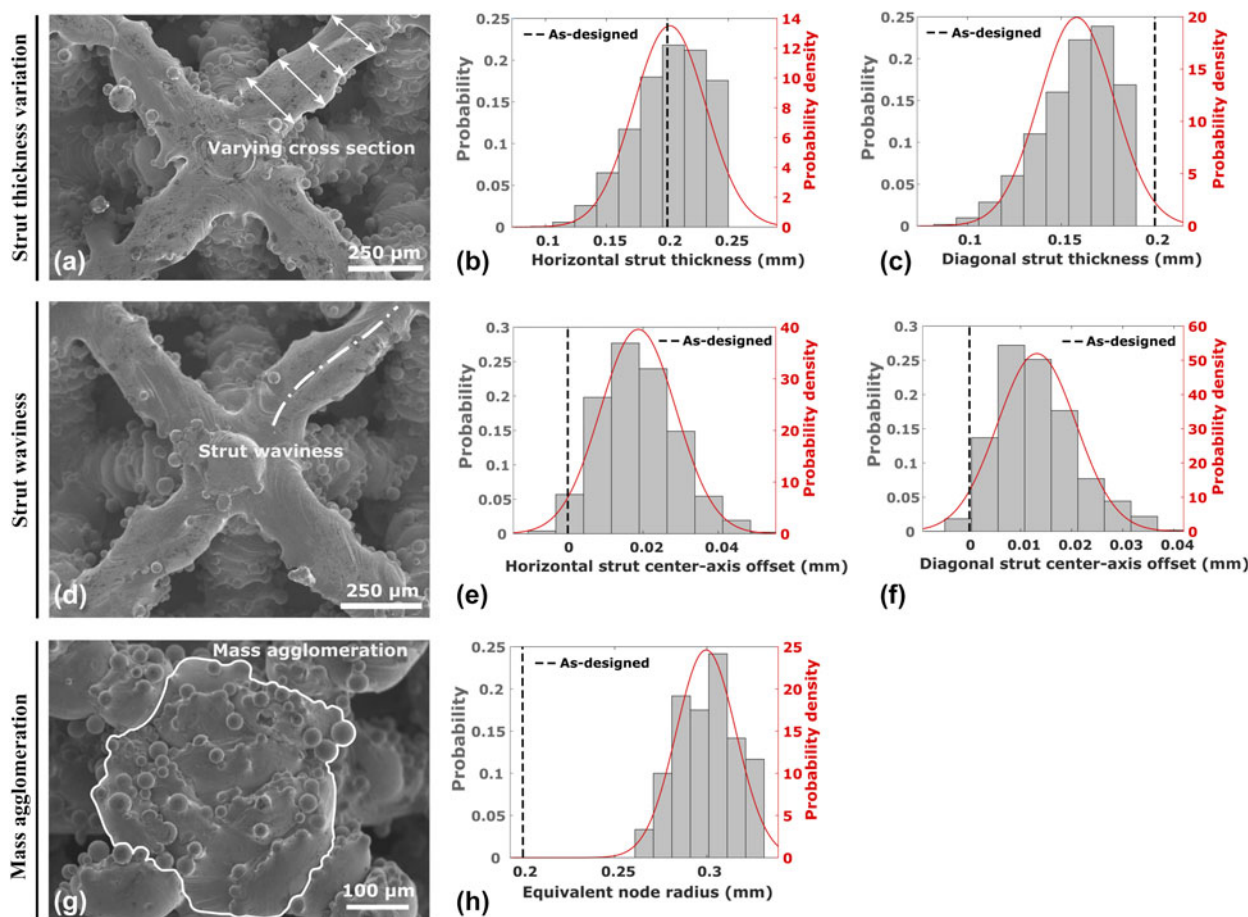


Figure 5: Characterization of morphological imperfections: (a) SEM observation of strut thickness variation along with probability distribution of thickness for (b) horizontal struts and (c) diagonal struts. (d) SEM observation of strut waviness along with probability distribution of center-axis offset for (e) horizontal struts and of (f) diagonal struts. (g) SEM observation of mass agglomeration at the node along with (h) probability distribution of equivalent node radius.

the average node oversizing, and the standard deviation $\sigma_n = 0.01$ mm corresponds to the severity of the variation of the equivalent node radius. Table SIII in the Supplementary material provides a summary of the morphological characterization of defects.

Numerical results

In this part, we present our findings from the numerical investigation on the impact of material property and morphological defects. The statistical distributions of as-manufactured defects obtained in the experimental investigation (Figs. 4 and 5) are integrated into computational models of imperfect architectures featuring dispersions of defects that are statistically representative of their as-built counterparts (Fig. 1). We expand the study by tuning the amplitude of the defects to generate as-designed imperfect models with as-designed defects that could correspond eventually to given parameters of the manufacturing processes. We use Asymptotic Homogenization

(AH) to compute the effective properties of the reconstructed models [44, 45].

Impact of material property defects

Even though geometrical imperfections have been extensively studied in the literature [24, 25, 26, 27, 28, 29, 30, 31, 32, 33, 34, 35, 36, 37, 38, 39, 40, 41, 42, 43, 44, 45, 46], the impact of material imperfections has remained so far unexplored. In this section, we study the sensitivity of the mechanical properties of the octet truss to as-manufactured and to as-designed material properties by examining the role of μ_E (mean value of Young's modulus) at the nodes and the diagonal struts with the goal of assessing their possible stiffening or softening effect. As noticed in the experimental results, AM typically induces material property values that are, except for the horizontal struts, higher than the expected nominal values provided from the manufacturer (equal to 114 GPa), and that are dependent on the location and the orientation.

Our numerical models incorporate three sets of material properties. To account for the material properties of the node,

a node oversizing was assumed with an as-built node radius to strut thickness ratio r/t equal to 2 with relative density prescribed to match the nominal value 0.27. The Young's modulus of the horizontal struts is maintained equal to its as-manufactured value (111 GPa). Figure 6 shows the sensitivity of the compressive Young's modulus along the Z direction to μ_E^n (mean value of Young's modulus of the node) and μ_E^d (mean value of Young's modulus of the diagonal strut). On the x and y axes are the normalized material properties μ_E^d/μ_{EN}^d and μ_E^n/μ_{EN}^n with respect to their nominal values μ_{EN}^d and μ_{EN}^n which represent the coordinates of the point N in Fig. 6.

Values of μ_E^n/μ_{EN}^n and μ_E^d/μ_{EN}^d lower (or higher) than 100% would infer softer (or stiffer) nodes and struts which can be obtained using other fabrication techniques. The color legend corresponds to the normalized effective compressive Young's modulus along the Z direction (building direction) with respect to the one of the as-designed lattice with nominal base material properties. In Fig. 6, point N and M correspond to the lattice with nominal properties and with as-manufactured material properties, respectively.

Figure 6 shows that the as-manufactured defects measured with AFM induce an increase of 105.5% over the nominal value. Points A, B, C, and D represent the boundaries of the domain and correspond to as-designed defects. (A) corresponds to the softening of the diagonal struts and of the nodes (70% of the nominal value). (B) visualizes the stiffening (130% of the nominal value) of the diagonal struts and the softening of the nodes (70% of the nominal value). (C) shows both amplified imperfections (130% of the nominal value). (D) shows material softening (70% of the nominal value) of the diagonal struts and material stiffening (130% of the nominal value) of the nodes. If both imperfections are amplified by 130%, the Young's modulus is predicted to increase by 115.3% of the nominal value; however, when they are decreased to 70%, the Young's modulus reduces to 59.5% of its nominal value.

The contour also shows that the stiffening of the diagonal struts to 130% of the nominal value and the softening of the nodes to 70% of the nominal value lead to a higher Young's modulus (86.4% of the nominal value) than for the stiffening of the nodes and the softening of the diagonal struts (84.4% of the nominal value). The increased stiffness of the nodes can impact the effective compressive Young's modulus due to the bending induced by the node radius to strut thickness ratio. In fact, if the lattice is purely stretching dominated, the increase of the stiffness of the node has minor effect on the Young's modulus [22].

Impact of morphological imperfections at the nodes

It is well recognized that strut imperfections influence the mechanical properties of lattice materials [29, 39, 40, 41, 42, 43,

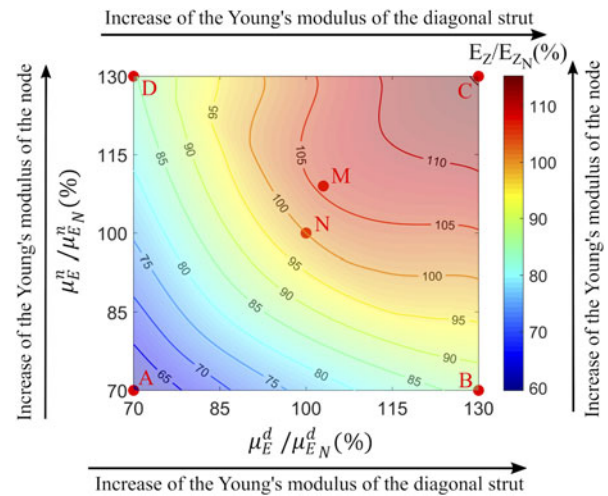


Figure 6: Contour plot for the normalized compressive Young's modulus of the lattice at nominal relative density. The x -axis and the y -axis represent the mean value of the Young's modulus of the diagonal strut and of the node normalized with respect to their nominal values. Points A, B, C, and D are representative points at the boundaries of the domain corresponding to as-designed material property imperfections. Point N represents the as-designed sample with nominal Young's modulus of the diagonal struts and of the nodes which are used as baseline for the normalization of the imperfect material properties. Point M represents the lattice with as manufactured material properties.

44, 45, 46, 47, 48, 49]. However, the sensitivity to mass agglomerations at the nodes has not been elucidated yet. At a given relative density, mass agglomerations correspond to redistributing the mass in the lattice and compensating the nodes oversizing by decreasing the thickness of the struts. Here, we examine the role of the node radius to strut to thickness ratio (r/t) at given values of relative density. For given struts thickness and nodes radius, the relative density can be expressed as:

$$\bar{\rho} = 1/L^3 \left(4 \left(4\pi r^3/3 - 2\pi t^2 \left(r - |r^2 - 0.25t^2|^{0.5} \right) \right) + 18.8t^2 \left(L/\sqrt{2} - 2|r^2 - 0.25t^2|^{0.5} \right) \right), \quad (1)$$

where $\bar{\rho}$, r , t , L are the relative density, the node radius, the struts thickness, and the unit cell length, respectively. In our analysis, the relevant material property is equal to its nominal value ($E = 114$ GPa).

Figure 7 shows the sensitivity of the compressive Young's modulus along the Z direction (see Fig. 1) to the mass agglomeration at the nodes (r/t) and to the relative density. On the x -axis is the normalized r/t with respect to its nominal value $(r/t)_N$ that corresponds to no mass agglomerations and the relative density appears on the y -axis. Values of r/t higher than 100% infer a node oversizing. The color legend corresponds to the normalized Young's modulus with respect to Young's modulus of the nominal lattice.

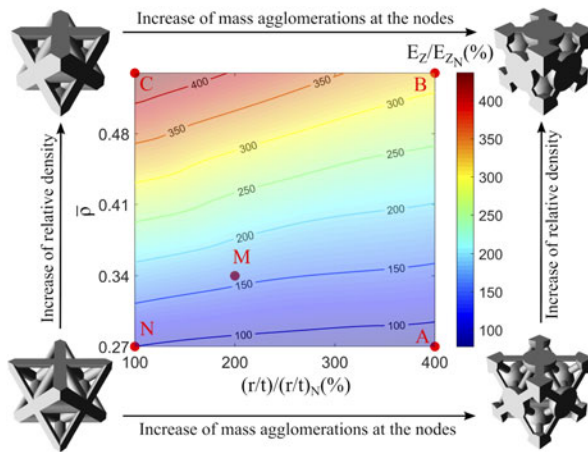


Figure 7: Contour plot for the normalized compressive Young's modulus of the lattice with nominal base material property (114 GPa). The x -axis and the y -axis represent the severity of mass agglomeration at the nodes and the relative density, respectively. Point N represents the nominal lattice without mass agglomerations and with a nominal relative density. Point M corresponds to the lattice with as-manufactured node oversizing and relative density.

Points N, A, B, and C in Fig. 7 are the boundaries of the domain. (N) represents the nominal unit cell without node oversizing and with a nominal relative density ($\bar{\rho} = 0.27$). (A) visualizes an amplified node oversizing (400% of the nominal value) at a nominal relative density ($\bar{\rho} = 0.27$). (B) shows an amplified node oversizing (400% of the nominal value) at increased relative density (200% of the nominal value). (C) shows the lattice without node oversizing at an increased relative density (200% of the nominal value). M corresponds to the as-manufactured lattice with a node oversizing $(r/t)_M = 2$ and relative density $\bar{\rho}_M = 0.34$.

At a fixed relative density equal to the nominal value, when the node oversizing is amplified by 400% of the nominal value, the Young's modulus is predicted to decrease to 78% of the value corresponding to the lattice without node oversizing. However, when the node radius to strut thickness ratio is amplified by the same amount (400%) at a higher relative density (200% of the nominal value), the Young's modulus is predicted to decrease to 73% of the value corresponding to the lattice without node oversizing. The result shows that the impact of node oversizing is more important at high values of relative density than at lower. Mass distribution, therefore, becomes crucial at low porosity than at high porosity. Furthermore, the result indicates that at high relative density, the effective Young's modulus does depend not only on the relative density [50] but also on mass distribution (r/t) . This is mainly due to the additional bending that is induced by the mass agglomerations at the nodes, a factor that contributes to switch the behaviour of the structure from a pure stretching to a combination of stretching and bending behaviour.

Impact of strut imperfections

Here, we examine the impact of strut waviness μ_o and strut thickness variation σ_t on the compressive Young's modulus along the Z direction (see Fig. 1) of the octet truss lattice. In our analysis, we prescribe the relative density at 0.27 by ensuring a compensation of strut thickness, i.e., when the horizontal struts are oversized (undersized), the diagonal struts are undersized or (oversized). Figure 8 shows five distinctive points. (N) corresponds to the nominal lattice, (A) the as-designed lattice without strut thickness variation and with amplified strut waviness (200% of the manufacturing value), (B) as-designed lattice with amplified strut thickness variation (200% of the manufacturing value) and amplified strut waviness (200% of the manufacturing value), (C) as-designed lattice without strut waviness and with an amplified strut thickness variation (200% of the manufacturing value), and (M) the as-manufactured lattice with as-manufactured strut thickness variation and strut waviness.

The x -axis and y -axis represent the severity of strut waviness and strut thickness variation, respectively, which are normalized with respect to the as-manufactured ones. The color legend corresponds to the normalized Young's modulus with respect to the nominal Young's modulus of the nominal lattice. The presence of as-manufactured defects leads to a decrease of 76.4% of the nominal value. If both imperfections are amplified by 200%, the Young's modulus reduces to 50% of the one of the nominal lattice. When taken independently, a 200% amplification of each defect has a different impact. Strut waviness penalizes more (67% of the one of the nominal lattice) than strut thickness variation (75% of the nominal value) because strut waviness induces additional bending in a stretching dominated structure [39].

Discussion

This work has shown the impact of defect type and magnitude on the mechanical properties of Ti-6Al-4V octet truss lattices. Because these defects typically appear combined in an as-built architecture, here, we discuss their individual and combined effect on their mechanical performance. Figure 9 shows a comparison of the compressive Young's modulus obtained experimentally and numerically by integrating single as-manufactured defects and their combination in the imperfect models along with the normalized deviation with respect to the experimental result.

The nominal model induces a 58% relative deviation with respect to the experimental data. When imperfections are introduced in the imperfect model, they can induce either a decrease or an increase of Young's modulus, an outcome dictated by the type of defect appearing either in the

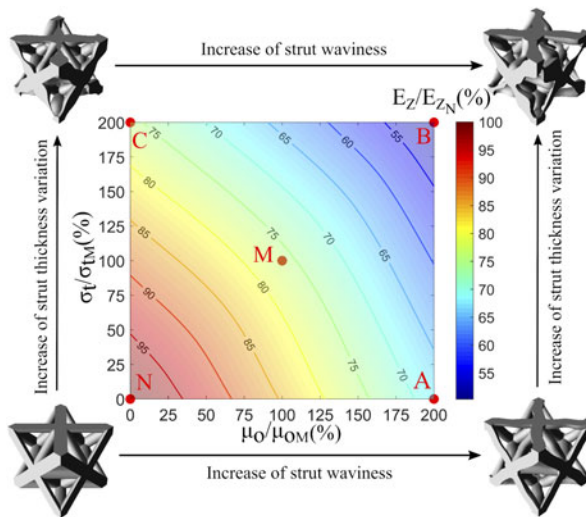


Figure 8: Contour plot for normalized Young's modulus of the lattice with nominal material property $E = 114$ GPa for a nominal relative density. The x-axis and the y-axis represent the severity of strut waviness and strut thickness variation, respectively. Point N represents the nominal lattice. Point M represents the lattice with as-manufactured parameters that are used as a baseline for parameter normalization.

morphology or in the base-material. The material property defects here investigated induce 60% relative deviation with respect to the experimental result. On the other hand, in a decreasing order, strut waviness followed by strut thickness variation, and node oversizing are the single defects that induce the smallest relative errors, quantified in percentage as 50%, 52%, and 54%, respectively.

The highest decrease of relative deviation from the experimental result is obtained when all morphological defects are combined in the imperfect models (40% deviation). This is followed by the combination of material property and morphological defects, and the combination of strut imperfections with a decrease in deviation of 43%, and 44%, respectively. This result shows that capturing the statistical representation of defects in imperfect models increases the accuracy of the model predictions.

Although this work studies the impact of two sets of defects (material property and morphological defects), the role of other sets of defects could be explored. For instance, the presence of porosity will most likely decrease the mechanical properties. However, the quantification of their extent clearly depends on the precision of the measurement tool. Bonded particles, which increase the mass of the lattice but do not contribute to the load-carrying capacity of the lattice, contribute also to a performance decrease.

The general methodology here presented for defect quantification and generation of imperfect models allows to predict the mechanical behavior of structures built with PBF processes. It thus represents a valuable tool to guide the design of structural components for given applications, such as bone replacement implants.

Conclusion

Imperfections induced by SLM were investigated in Ti-6Al-4V octet truss lattice materials. The conclusions that can be drawn from our experimental and numerical study are as follows:

- (1) Surface defects mainly appeared in the form of bonded particles. With an average size of $40\text{ }\mu\text{m}$, they affected the surface quality of the fabricated parts.
- (2) Microstructural defects in the form of pores, cracks, and poor bonding defects were observed mainly in the struts. Significant local variations of the texture were observed within the lattice. The texture was found to depend on the strut orientation, and a strong texture was obtained at nodes in the (0001) plane where the MUD reached 14.78.
- (3) A method involving AFM enabled to obtain a statistical distribution of material property defects, thereby showing important spatial variations of material properties within the lattice. The nodes possessed the highest average Young's modulus, which was approximately 13% higher than the one of the horizontal struts and 6% higher than that of the diagonal struts. Apart from the horizontal struts, SLM induced higher material properties than the nominal values provided by the manufacturer.
- (4) Combined as-manufactured morphological defects induced a decrease of Young's modulus to 70% of the one of the nominal lattice, whereas as-manufactured material property defects induced an increase of Young's modulus to 105.5% of the nominal value.
- (5) The impact of node oversizing was assessed more important at high than at low values of relative density, with 73% decrease of Young's modulus at $\bar{\rho} = 0.54$ in comparison with 78% decrease of Young's modulus at $\bar{\rho} = 0.27$ for a node oversizing $r/t = 4$.
- (6) In decreasing order, the strut waviness, the strut thickness variation, and the node oversizing were single defects that reduced Young's modulus to 84.63%, 88%, and 91% of the one of the nominal lattice, respectively. When all morphological defects were integrated, the Young's modulus decreased to 70% of the nominal value, which corresponded to the lowest relative deviation from experiments (40%). This result shows that adequate statistical distributions of as-manufactured defects in the models can provide a more accurate assessment of the realistic behavior of as-built lattice materials.

Methods

Mechanical testing

10 manufactured replicates corresponding to the design point M were tested in the linear regime in compression on

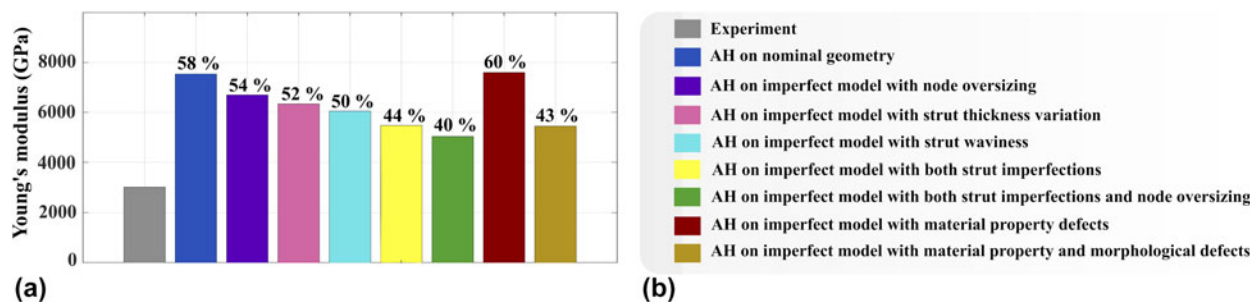


Figure 9: Comparison of Young's modulus obtained experimentally and numerically: (a) The histogram with relative deviation calculated with respect to the baseline experimental result are presented along with (b) the pertinent legend.

a 50 kN servo-electric machine with a constant strain rate equal to 0.01 s^{-1} to obtain their compressive elastic modulus along the building direction [Fig. 1(b)] as following ISO-13314 standard. An extensometer mounted on the samples measured the strain.

Material property characterization

A JPK atomic force microscope (JPK Nano-wizard@3 Bio-Science, Berlin, Germany) was used to conduct nano-indentation test on the polished transverse sections. The surface of the samples was polished to minimize the surface roughness ($<5 \text{ nm}$). The cut sections were fixed on microscope glass slides using a double-sided tape. Non-contact high resonance (NCHR) cantilevers (Nanotools USA LLC, Henderson, NV) with a resonance frequency of 330 kHz, nominal spring constant of 40 N/m, and integrated spherical tip of radius 50 nm ($\pm 10\%$) were used for imaging.

A handcrafted natural diamond Nano indenting tip (DNISP-HS; Bruker, Mannheim, Germany) with a defined spherical tip of radius $R = 50 \text{ nm} \pm 10\%$ and a spring constant of 600 N/m was used to indent the surface of the samples. The indentation depth δ was selected to be less than 10 nm to avoid inelastic deformations. The deflection sensitivity of the piezo module was established by probing the surface of the glass. The stiffness of the cantilever was calibrated before the tests. The slope of the retracting curve was fit to $S = dF/d\delta = 2E\sqrt{R\delta}/(1 - \nu^2)$ to yield the elastic modulus E . The deformation of the sample relative to its thickness and relative to the radius of the probe was very small. Poisson's ratio ν was selected as 0.342. Data analysis was performed with the JPK data processing software. Relevant indentation data are summarized in Table SII in the Supplementary material.

Characterization of morphological defects

The morphological characterization consists in finding the center-axis and the varying thickness of the struts, and the nodes radii. The CT-reconstructed lattice [Fig. 1(c)] was discretized with a surface mesh. Then, the horizontal struts, the diagonal struts, and the nodes were isolated to find their

morphological characteristics [Fig. 1(d)]. To determine the strut thickness variation [Fig. 1(e)], a series of planes were designed to intersect the strut. On the intersection plane, the cross-section radius and center were fitted using the least squares method [51]. The center-axis is then determined by joining the cross-sections centers [Fig. 1(e)]. The center-axis deviation corresponds to the deviation of the determined center-axis from the ideal one. The node radius [Fig. 1(f)] is extracted by determining the radius r of the sphere with a volume that is equal to that of the mass agglomeration: $r = (3V/(4\pi))^{1/3}$, where V is the volume of the isolated mass agglomeration at the node. To obtain an accurate statistical distribution of defects, at least 150 nodes, 150 horizontal struts, and 150 diagonal struts were randomly isolated from the samples and were analyzed using the described method.

Numerical methods

Two sets of finite element models were constructed using the commercial software package ABAQUS (Dassault Systemes Simulia Corp, France):

- Statistical models: The probability distributions of the measured defects built in the experimental methods were used as an input to build multiple statistical models, each with statistical values of the defects sampled at random (Fig. 1). To model strut imperfections [Fig. 1(e)], each strut was divided into 5 sections characterized by a varying thickness with statistical distribution parameters (μ_t , σ_t) and an offset from the nominal center-axis position with statistical distribution parameters (μ_o , σ_o). A sphere was modeled at the intersection of the struts representing the mass agglomeration at the node with statistical parameters (μ_n , σ_n) [Fig. 1(f)]. Three sets of isotropic material properties with statistical values obtained from AFM analysis were dispersed with respect to the location of node (μ_E^n), horizontal struts (μ_E^h), and diagonal struts (μ_E^d). A Python-ABAQUS script was used to introduce the distributed sets of morphological and material property defects into the numerical models.

- (ii) As-designed models: The second set of models integrate as-designed defects and were used to unveil the impact of each type and magnitude of defect on the mechanical properties of the octet truss lattice.

Because of the low slenderness of the struts that constitute our models, ten-node tetrahedral elements (C_3D_{10}) were used to mesh the parts. To reduce the computation time required by the full discretized lattice, periodic boundary conditions were assumed on a single unit cell. Asymptotic homogenization was performed on the representative volume element to find the effective compressive Young's modulus [52].

Acknowledgments

The authors acknowledge funding from the Natural Sciences and Engineering Research Council of Canada through the Discovery Grant Program and the Network for Holistic Innovation in Additive Manufacturing. The Canadian Foundation for Innovation (Grant No. 229251) is also acknowledged.

Supplementary material

To view supplementary material for this article, please visit <https://doi.org/10.1557/jmr.2020.75>.

References:

1. S.J. Hollister: Scaffold design and manufacturing: From concept to clinic. *Adv. Mater.* **21**, 3330–3342 (2009).
2. S.J. Hollister and W.L. Murphy: Scaffold translation: Barriers between concept and clinic. *Tissue Eng., Part B* **17**, 459–474 (2011).
3. B. Levine: A new era in porous metals: Applications in orthopaedics. *Adv. Eng. Mater.* **10**, 788–792 (2008).
4. G. Ryan, A. Pandit, and D.P. Apatsidis: Fabrication methods of porous metals for use in orthopaedic applications. *Biomaterials* **27**, 2651–2670 (2006).
5. O.L.A. Harrysson, O. Cansizoglu, D.J. Marcellin-Little, D.R. Cormier, and H.A. West, II: Direct metal fabrication of titanium implants with tailored materials and mechanical properties using electron beam melting technology. *Mater. Sci. Eng., C* **28**, 366–373 (2008).
6. P. Heintz, L. Müller, C. Körner, R.F. Singer, and F.A. Müller: Cellular Ti–6Al–4V structures with interconnected macro porosity for bone implants fabricated by selective electron beam melting. *Acta Biomater.* **4**, 1536–1544 (2008).
7. L. Mullen, R.C. Stamp, W.K. Brooks, E. Jones, and C.J. Sutcliffe: Selective laser melting: A regular unit cell approach for the manufacture of porous, titanium, bone in-growth constructs, suitable for orthopedic applications. *J. Biomed. Mater. Res., Part B* **89**, 325–334 (2009).
8. L.E. Murr, S.M. Gaytan, F. Medina, H. Lopez, E. Martinez, B.I. Machado, D.H. Hernandez, L. Martinez, M.I. Lopez, and R.B. Wicker: Next-generation biomedical implants using additive manufacturing of complex, cellular, and functional mesh arrays. *Philos. Trans. R. Soc., A* **368**, 1999–2032 (2010).
9. Y.J. Liu, S.J. Li, H.L. Wang, W.T. Hou, Y.L. Hao, R. Yang, T.B. Sercombe, and L.C. Zhang: Microstructure, defects, and mechanical behavior of beta-type titanium porous structures manufactured by electron beam melting and selective laser melting. *Acta Mater.* **113**, 56–67 (2016).
10. H. Gong, K. Rafi, H. Gu, T. Starr, and B. Stucker: Analysis of defect generation in Ti–6Al–4V parts made using powder bed fusion additive manufacturing processes. *Addit. Manuf.* **1–4**, 87–98 (2014).
11. I. Echeta, X. Feng, B. Dutton, S. Piano, and R. Leach: Review of defects in lattice structures manufactured by powder bed fusion. *Int. J. Adv. Manuf. Technol.* **106**, 2649–2668 (2019).
12. T. Tancogne-Dejean, A.B. Spierings, and D. Mohr: Additively-manufactured metallic micro-lattice materials for high specific energy absorption under static and dynamic loading. *Acta Mater.* **116**, 14–28 (2016).
13. A. Ferrigno, F. Di Caprio, R. Borrelli, F. Auricchio, and A. Vigliotti: The mechanical strength of Ti–6Al–4V columns with regular octet microstructure manufactured by electron beam melting. *Materialia* **5**, 100232 (2019).
14. S. Chen and P. Isaksson: A note on the defect sensitivity of brittle solid foams. *Eng. Fract. Mech.* **206**, 541–550 (2019).
15. S. Chen and P. Isaksson: An experimental analysis of the defect sensitivity of solid foams. *Theor. Appl. Fract. Mech.* **96**, 768–774 (2018).
16. B. Zhang, Y. Li, and Q. Bai: Defect formation mechanisms in selective laser melting: A review. *Chin. J. Mech. Eng.* **30**, 515–527 (2017).
17. Y. Amani, S. Dancette, P. Delroisse, A. Simar, and E. Maire: Compression behavior of lattice structures produced by selective laser melting: X-ray tomography based experimental and finite element approaches. *Acta Mater.* **159**, 395–407 (2018).
18. Z. Dong, Y. Liu, W. Li, and J. Liang: Orientation dependency for microstructure, geometric accuracy and mechanical properties of selective laser melting AlSi10Mg lattices. *J. Alloys Compd.* **791**, 490–500 (2019).
19. C. Yan, L. Hao, A. Hussein, and D. Raymont: Evaluations of cellular lattice structures manufactured using selective laser melting. *Int. J. Mach. Tool Manufact.* **62**, 32–38 (2012).
20. Z.S. Bagheri, D. Melancon, L. Liu, R.B. Johnston, and D. Pasini: Compensation strategy to reduce geometry and mechanics mismatches in porous biomaterials built with selective laser melting. *J. Mech. Behav. Biomed. Mater.* **70**, 17–27 (2017).
21. D. Melancon, Z.S. Bagheri, R.B. Johnston, L. Liu, M. Tanzer, and D. Pasini: Mechanical characterization of structurally porous biomaterials built via additive manufacturing: Experiments, predictive models, and design maps for load-bearing bone replacement implants. *Acta Biomater.* **63**, 350–368 (2017).

22. D.M.K. Carlos, M. Portelaa, and J.R. Greera: Impact of node geometry on the effective stiffness of non-slender three-dimensional truss lattice architectures. *Extreme Mech. Lett.* **22**, 138–148 (2018).
23. S. Arabnejad, R. Burnett Johnston, J.A. Pura, B. Singh, M. Tanzer, and D. Pasini: High-strength porous biomaterials for bone replacement: A strategy to assess the interplay between cell morphology, mechanical properties, bone ingrowth, and manufacturing constraints. *Acta Biomater.* **30**, 345–356 (2016).
24. L. Liu, P. Kamm, F. García-Moreno, J. Banhart, and D. Pasini: Elastic and failure response of imperfect three-dimensional metallic lattices: The role of geometric defects induced by selective laser melting. *J. Mech. Phys. Solids* **107**, 160–184 (2017).
25. A. Ataee, Y. Li, D. Fraser, G. Song, and C. Wen: Anisotropic Ti–6Al–4V gyroid scaffolds manufactured by electron beam melting (EBM) for bone implant applications. *Mater. Des.* **137**, 345–354 (2018).
26. X. Liu and N. Liang: Effective elastic moduli of triangular lattice material with defects. *J. Mech. Phys. Solids* **60**, 1722–1739 (2012).
27. A. Gross, P. Pantidis, K. Bertoldi, and S. Gerasimidis: Correlation between topology and elastic properties of imperfect truss-lattice materials. *J. Mech. Phys. Solids* **124**, 577–598 (2019).
28. A.E. Simone and L.J. Gibson: The effects of cell face curvature and corrugations on the stiffness and strength of metallic foams. *Acta Mater.* **46**, 3929–3935 (1998).
29. C. Chen, T.J. Lu, and N.A. Fleck: Effect of imperfections on the yielding of two-dimensional foams. *J. Mech. Phys. Solids* **47**, 2235–2272 (1999).
30. N.E.R. Romijn and N.A. Fleck: The fracture toughness of planar lattices: Imperfection sensitivity. *J. Mech. Phys. Solids* **55**, 2538–2564 (2007).
31. D. Pasini and J.K. Guest: Imperfect architected materials: Mechanics and topology optimization. *MRS Bull.* **44**, 766–772 (2019).
32. P.E. Seiler, H.C. Tankasala, and N.A. Fleck: Creep failure of honeycombs made by rapid prototyping. *Acta Mater.* **178**, 122–134 (2019).
33. A. Cuadrado, A. Yáñez, O. Martel, S. Deviaene, and D. Monopoli: Influence of load orientation and of types of loads on the mechanical properties of porous Ti6Al4V biomaterials. *Mater. Des.* **135**, 309–318 (2017).
34. S.L. Sing, F.E. Wiria, and W.Y. Yeong: Selective laser melting of lattice structures: A statistical approach to manufacturability and mechanical behavior. *Robot. Comput. Integrated Manuf.* **49**, 170–180 (2018).
35. C.-Y. Lin, T. Wirtz, F. LaMarca, and S.J. Hollister: Structural and mechanical evaluations of a topology optimized titanium interbody fusion cage fabricated by selective laser melting process. *J. Biomed. Mater. Res., Part A* **83A**, 272–279 (2007).
36. O. Al-Ketan, R. Rowshan, and R.K. Abu Al-Rub: Topology-mechanical property relationship of 3D printed strut, skeletal, and sheet based periodic metallic cellular materials. *Addit. Manuf.* **19**, 167–183 (2018).
37. C. Han, Y. Li, Q. Wang, S. Wen, Q. Wei, C. Yan, L. Hao, J. Liu, and Y. Shi: Continuous functionally graded porous titanium scaffolds manufactured by selective laser melting for bone implants. *J. Mech. Behav. Biomed. Mater.* **80**, 119–127 (2018).
38. M. Asgari, J. Abi-Rafeh, G.N. Hendy, and D. Pasini: Material anisotropy and elasticity of cortical and trabecular bone in the adult mouse femur via AFM indentation. *J. Mech. Behav. Biomed. Mater.* **93**, 81–92 (2019).
39. D.D. Symons and N.A. Fleck: The imperfection sensitivity of isotropic two-dimensional elastic lattices. *J. Appl. Mech.* **75**, 51011–51018 (2008).
40. C. Chen, T.J. Lu, and N.A. Fleck: Effect of inclusions and holes on the stiffness and strength of honeycombs. *Int. J. Mech. Sci.* **43**, 487–504 (2001).
41. A.E.E. Simone and L.J.J. Gibson: Effects of solid distribution on the stiffness and strength of metallic foams. *Acta Mater.* **46**, 2139–2150 (1998).
42. N.A. Fleck and X. Qiu: The damage tolerance of elastic–brittle, two-dimensional isotropic lattices. *J. Mech. Phys. Solids* **55**, 562–588 (2007).
43. V.S. Deshpande, M.F. Ashby, and N.A. Fleck: Foam topology: Bending versus stretching dominated architectures. *Acta Mater.* **49**, 1035–1040 (2001).
44. A.L. Kalamkarov, I.V. Andrianov, and V.V. Danishevs'kyy: Asymptotic homogenization of composite materials and structures. *Appl. Mech. Rev.* **62**, 030802 (2009).
45. S.J. Hollister and N. Kikuchi: A comparison of homogenization and standard mechanics analyses for periodic porous composites. *Comput. Mech.* **10**, 73–95 (1992).
46. J.C. Wallach and L.J. Gibson: Defect sensitivity of a 3D truss material. *Scr. Mater.* **45**, 639–644 (2001).
47. M. Dallago, B. Winiarski, F. Zanini, S. Carmignato, and M. Benedetti: On the effect of geometrical imperfections and defects on the fatigue strength of cellular lattice structures additively manufactured via selective laser melting. *Int. J. Fatigue* **124**, 348–360 (2019).
48. M. Dallago, M. Benedetti, V. Luchin, and V. Fontanari: Orthotropic elastic constants of 2D cellular structures with variously arranged square cells: The effect of filleted wall junctions. *Int. J. Mech. Sci.* **122**, 63–78 (2017).
49. D.T.D. Queheillalt, V.V.S. Deshpande, and H.N.G.H. Wadley: Truss waviness effects in cellular lattice structures. *J. Mech. Mater. Struct.* **2**, 1657–1675 (2007).
50. L.J. Gibson: The Elastic and Plastic Behaviour of Cellular Materials. Doctoral thesis. University of Cambridge (1981).
51. S.J. Ahn, W. Rauh, and H.-J. Warnecke: Least-squares orthogonal distances fitting of circle, sphere, ellipse, hyperbola, and parabola. *Pattern Recogn.* **34**, 2283–2303 (2001).
52. C.V. Le, P.H. Nguyen, H. Askes, and D.C. Pham: A computational homogenization approach for limit analysis of heterogeneous materials. *Int. J. Numer. Methods Eng.* **112**, 1381–1401 (2017).